View metadata, citation and similar papers at core.ac.uk

brought to you by CORE

provided by epublications@Marquette

Marquette University
e-Publications@Marquette

Electrical and Computer Engineering Faculty Research and Publications

Electrical and Computer Engineering, Department of

5-7-2019

Computationally Efficient Optimization of a Five-Phase Flux-Switching PM Machine Under Different Operating Conditions

Hao Chen
Beijing Institute of Technology

Xiangdong Liu
Beijing Institute of Technology

Nabeel Demerdash
Marquette University, nabeel.demerdash@marquette.edu

Ayman M. EL-Refaie
Marquette University, ayman.el-refaie@marquette.edu

Zhen Chen
Beijing Institute of Technology

See next page for additional authors

Accepted version. *IEEE Transactions on Vehicular Technology*, Vol. 68, No. 7 (July 2019): 6495 - 6508. DOI. © 2019 IEEE. Used with permission.

Authors
Hao Chen, Xiangdong Liu, Nabeel Demerdash, Ayman M. EL-Refaie, Zhen Chen, and Jiangbiao He

Marquette University

e-Publications@Marquette

Electrical Engineering Faculty Research and Publications/College of Arts and Sciences

***This paper is NOT THE PUBLISHED VERSION;* but the author's final, peer-reviewed manuscript.** The published version may be accessed by following the link in the citation below.

IEEE Transactions on Vehicular Technology, Vol. 68, No. 7 (July 2019): 6495-6508. DOI. This article is © IEEE and permission has been granted for this version to appear in e-Publications@Marquette. IEEE does not grant permission for this article to be further copied/distributed or hosted elsewhere without the express permission from IEEE.

Computationally Efficient Optimization of a Five-Phase Flux-Switching PM Machine Under Different Operating Conditions

Hao Chen
School of Automation, Beijing Institute of Technology, BeijingChina

Xiangdong Liu
School of Automation, Beijing Institute of Technology, Beijing, China

Nabeel A.O. Demerdash
Department of Electrical and Computer Engineering, Marquette University, Milwaukee, WI, USA

Ayman M. EL-Refaie
Department of Electrical and Computer Engineering, Marquette University, Milwaukee, WI, USA

Zhen Chen
School of Automation, Beijing Institute of Technology, Beijing, China

Jiangbiao He
Department of Electrical and Computer Engineering, University of Kentucky, Lexington, KY, USA

ABSTRACT

This paper investigates the comparative design optimizations of a five-phase outer-rotor flux-switching permanent magnet (FSPM) machine for in-wheel traction applications. To improve the comprehensive performance of the motor, two kinds of large-scale design optimizations under different operating conditions are performed and compared, including the traditional optimization performed at the rated operating point and the optimization targeting the whole driving cycles. Three driving cycles are taken into account, namely, the urban dynamometer driving schedule (UDDS), the highway fuel economy driving schedule (HWFET), and the combined UDDS/HWFET, representing the city, highway, and combined city/highway driving, respectively. Meanwhile, the computationally efficient finite-element analysis (CE-FEA) method, the cyclic representative operating points extraction technique, as well as the response surface methodology (in order to minimize the number of experiments when establishing the inverse machine model), are presented to reduce the computational effort and cost. From the results and discussion, it will be found that the optimization results against different operating conditions exhibit distinct characteristics in terms of geometry, efficiency, and energy loss distributions. For the traditional optimization performed at the rated operating point, the optimal design tends to reduce copper losses but suffer from high core losses; for UDDS, the optimal design tends to minimize both copper losses and PM eddy-current losses in the low-speed region; for HWFET, the optimal design tends to minimize core losses in the high-speed region; for the combined UDDS/HWFET, the optimal design tends to balance/compromise the loss components in both the low-speed and high-speed regions. Furthermore, the advantages of the adopted optimization methodologies versus the traditional procedure are highlighted.

SECTION I. Introduction

As the most important component in the traction system of electric vehicles (EVs), electric machines should be designed to have high torque density to provide the required acceleration capability in the low-speed region, and high flux-weakening capability to expand the constant-power speed range in the high-speed region. Compared to the conventional machine topologies commonly used in this application, e.g., induction motors [1], switched reluctance motors [2], and permanent magnet synchronous motors (PMSM) [3], flux-switching permanent magnet (FSPM) machines have attracted more attention due to their simple and robust rotor, high torque density, and favorable thermal dissipation [4].

Recently, FSPM machines with various configurations such as original configurations [5], C- and E-core configurations [6], have been presented for a diversity of applications. However, most of these configurations are limited to three-phase inner-rotor machines. Multi-phase motors have shown advantages in terms of their fault-tolerance capability, low torque pulsation, and additional degrees of freedom in the associated control system [7]. Moreover, outer-rotor motors are more suitable for in-wheel traction due to their compact and space-saving constructions, low acoustic noise, and high transmission efficiency with direct-drive technology. Therefore, a five-phase outer-rotor FSPM machine with E-core stator is built and analyzed in this paper. Other number of phases system including six-phase, twelve-phase systems, is beyond the scope of this paper and will be investigated in a future work.

Design optimization of FSPM machines is a timely topic that has received continued attention. Ref. [8] proposed an multi-objective design optimization strategy for a flux-switching machine used in wind energy generators. In ref. [9], a multi-objective optimization of a 6/22 stator/rotor pole FSPM motor was designed to minimize the cogging torque and torque ripple. In ref. [10], a double mechanical port FSPM machine is optimized by genetic algorithm, in which, the average torque, the torque ripple, and the magnetic coupling between the inner and

outer motors are considered as three objectives. In ref. [11], a systematic multi-level optimization is proposed to reduce the torque ripple of a FSPM motor, including both motor level and control level. However, in these previous optimization studies, only the rated operating point was taken into consideration, while the performance of motor in the expanded speed range is neglected, even though the flux-weakening capability is very important for traction applications.

On the other hand, the actual motor in EV applications operates at very dynamic torque-speed combinations over short periods of time, and it may behave differently in various driving conditions. Hence, it is necessary to consider the practical working conditions during the design procedure of such motors. Recently, researchers began to evaluate the performance of motors over a specific driving cycle [12]–[13][14][15]. The influence of geometrical parameters of a surface-mounted PM motor on the iron and copper losses over the New European Drive Cycle (NEDC) are reported in [12], it shows that a higher inductance and lower flux density in stator core can significantly reduce the total energy losses over the NEDC. Energy consumption instead of static efficiency map is evaluated for an induction motor and an interior PMSM during the Federal Urban Drive Schedule (FUDS) in [13]. The cyclic representative points method was implemented to optimize a PM-assisted synchronous reluctance motor considering two U.S. driving cycles in [14]. A large-scale design optimization for the Toyota Prius interior PM motor under a compound driving cycle consisting of common U.S. driving schedules was developed in [15]. As is known, the optimization limited to steady-state performance does not necessarily lead to optimal solution for the whole driving cycle. Likewise, a design optimized against a driving cycle does not yield the best performance when a different driving cycle or condition takes place. However, the comparison of optimizations under different operating conditions has seldom been assessed.

This paper contains new contributions to the subject matter by demonstrating an automated large-scale optimization procedure for a five-phase FSPM machine under different operating conditions, including the traditional optimization performed at the rated operating point, and the optimization targeting the whole driving cycle. Moreover, a systematic comparative study on the optimal designs is established based on three different driving cycles, i.e., Urban Dynamometer Driving Schedule (UDDS), Highway Fuel Economy Driving Schedule (HWFET), and the combined UDDS/HWFET, representing the city, highway, and combined city/highway driving conditions, respectively. Other new elements of interest include several techniques to reduce the computational burden during the optimization, e.g., the extension of a computationally efficient finite-element analysis (CE-FEA) for the five-phase FSPM machine; the representative operating points technique for the actual driving cycle; and the response surface methodology in order to minimize the number of experiments when establishing the inverse machine model.

Accordingly, this paper consists of six sections. The CE-FEA methodology is extended for the five-phase FSPM machine in Section II. Section III describes the investigated driving cycles and the associated techniques to extract the representative operating points and calculate the armature currents for these operating points. Section IV covers the optimization strategy and the associated objectives, constraints, as well as fitness functions. The optimization results together with comparison and discussion are presented in Section V. Finally, Section VI is dedicated to the conclusions.

SECTION II. Computationally Efficient FEA and Experimental Validation

For the large-scale optimization, it is imperative to verify the reliability of the electromagnetic analysis method for the performance evaluation of the motor. An initial machine prototype design of a FSPM machine is utilized to verify the reliability of this electromagnetic machine modeling approach.

A. Topology of the Five-Phase FSPM Machine Prototype

A five-phase outer-rotor FSPM machine with 10 stator poles and 21 rotor teeth was initially designed and manufactured for an in-wheel traction application as shown in Fig. 1. The E-core topology is used due to its

advantages of higher torque density and better flux-weakening capability, compared with conventional topologies [16]. Its main parameters are listed in Table I.

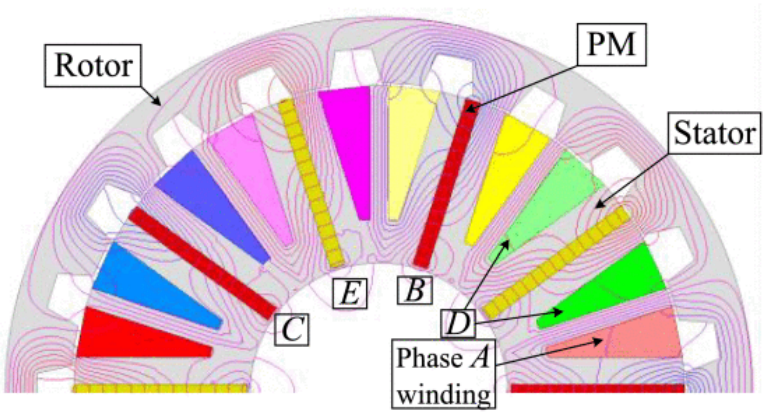

Fig. 1. Cross-section of the initially designed five-phase FSPM machine.

TABLE I Main Parameters of the FSPM Machine

Parameter	Value	Parameter	Value
Supply voltage (VDC)	400	Stator outer radius (mm)	91.48
Rated phase current (A)	10	Stator inner radius (mm)	38.72
Rated speed (r/min)	500	Stack length (mm)	66
Rotor outer radius (mm)	112.5	Number of turns/phase	130
Rotor inner radius (mm)	92.76	PM remanence NdFeB(T)	1.23
Air-gap height (mm)	0.92	Silicon steel sheet	C35A300

B. CE-FEA

It is well known that FSPM machines are highly nonlinear due to their strong magnetic saturation. Consequently, a substantial effort for accurate electromagnetic analysis is required. Whereas large-scale optimizations, which involve thousands of candidate designs, call for fast computations. Recently, some novel methodologies, e.g., CE-FEA [17]–[18] and the so-called "Pseudo Rotating Superposition (PRS)" [19], offer an effective solution for fast and high-fidelity simulation. These approaches were originally developed for three-phase PM motors. In this part, the CE-FEA method will be extended to five-phase FSPM Machines.

The CE-FEA is ultrafast because it fully exploits the electric and magnetic symmetry and periodicity of electric machines. For an m-phase machine, m equidistantly space samples of flux linkage, λ, can be provided by a single magnetostatic FE solution. Taking the five-phase motor as an example, it is expressed by eq. (1). Furthermore, the number of samples is doubled based on the half-wave symmetry by eq. (2). Thus, $n \times m \times 2$samples are constructed by n magnetostatic FE solutions. Then, the outputs including flux linkages, back-electromotive forces (EMFs), torque, and losses are obtained by post-processing techniques. As well known, post-processing in MATLAB software is much more time-saving than the FE solutions in ANSYS software. Therefore, the CE-FEA is much more computationally efficient than the conventional time-stepping (TS) FEA.

$$\left.\begin{aligned}\lambda_a(\theta) &= \lambda_a(\theta)\\ \lambda_a(\theta+72^\circ) &= \lambda_e(\theta)\\ \lambda_a(\theta+2\times72^\circ) &= \lambda_d(\theta)\\ \lambda_a(\theta+3\times72^\circ) &= \lambda_c(\theta)\\ \lambda_a(\theta+4\times72^\circ) &= \lambda_b(\theta)\end{aligned}\right\} \quad (1)(2)$$

$$\lambda(\theta) = -\lambda(\theta+180^\circ)$$

Fig. 2 and Fig. 3 show the reconstruction procedure of the flux linkage and torque profiles, respectively. For comparison, the results from TS-FEA are also presented in these two figures as marked with blue lines. Three basic steps are included in this procedure: 1) 6 points during the range of 0–36° are obtained by FE solutions. 2) 24 points are obtained with post-processing technique by eq. (1) based on the electric circuit symmetry. 3) 30 points are obtained also with post-processing technique by the half-wave symmetry, eq. (2). It should be noted that under load condition, all of the five-phase armature windings are energized according to eq. (3).

$$\left.\begin{aligned}i_a(t) &= \sqrt{2}I\cdot\sin(\omega_e\cdot t)\\ i_b(t) &= \sqrt{2}I\cdot\sin\left(\omega_e\cdot t-\frac{2\pi}{5}\right)\\ i_c(t) &= \sqrt{2}I\cdot\sin\left(\omega_e\cdot t-\frac{4\pi}{4}\right)\\ i_d(t) &= \sqrt{2}I\cdot\sin\left(\omega_e\cdot t-\frac{6\pi}{5}\right)\\ i_e(t) &= \sqrt{2}I\cdot\sin\left(\omega_e\cdot t-\frac{8\pi}{5}\right)\end{aligned}\right\} \quad (3)$$

where, *I* is the phase current rms value, ωe is the motor speed in electrical rad/s. The results obtained by CE-FEA and TS-FEA are summarized in Table II. In which, λ_1 is the fundamental component of flux linkage, *THD* is its total harmonic distortion, T_{avg} is the average torque, and T_{rip} is the torque ripple. As observed, the results from CE-FEA and TS-FEA are in good agreement, while the computational time of CE-FEA is significantly reduced. The advantage of CE-FEA is imperative for large-scale optimization.

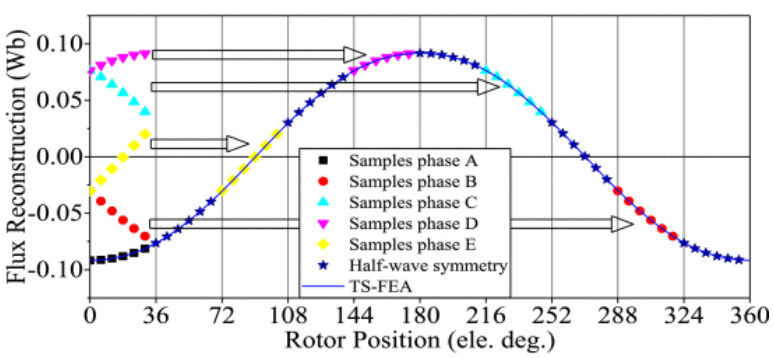

Fig. 2. Flux reconstruction procedure of the five-phase FSPM machine.

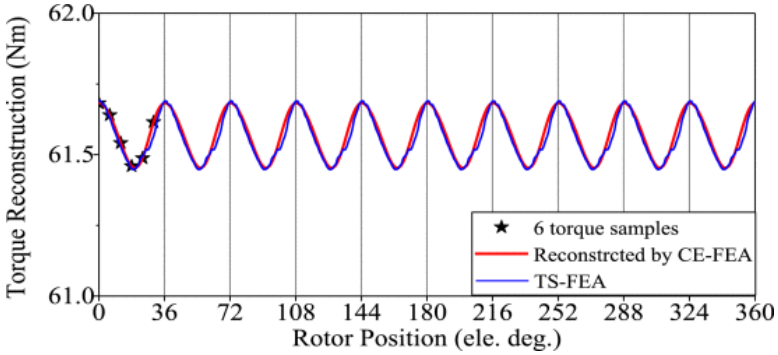

Fig. 3. Torque reconstruction procedure of the five-phase FSPM machine.

TABLE II. Comparison of Results From CE-FEA and TS-FEA

	Flux linkage		**Torque**		
	λ_1 (Wb)	***THD***	**T_{avg} (Nm)**	**T_{rip}**	**Computational time (s)**
CE-FEA	0.09354	1.723%	61.57	0.37%	68
TS-FEA	0.09352	1.721%	61.56	0.39%	622

C. Reliability Verification of the FEA-Based Analysis

Fig. 4 illustrates the prototype of the FSPM machine (the geometrical parameters of the prototyped motor are summarized in Table I). It should be mentioned that to ease the manufacturing process and improve the mechanical strength, 1-mm flux ribs at the inner edges of the PMs and 3-mm bulges into the stator bolster are included in the stator [see Fig. 4(b)]. The test hardware setup is shown in Fig. 5.

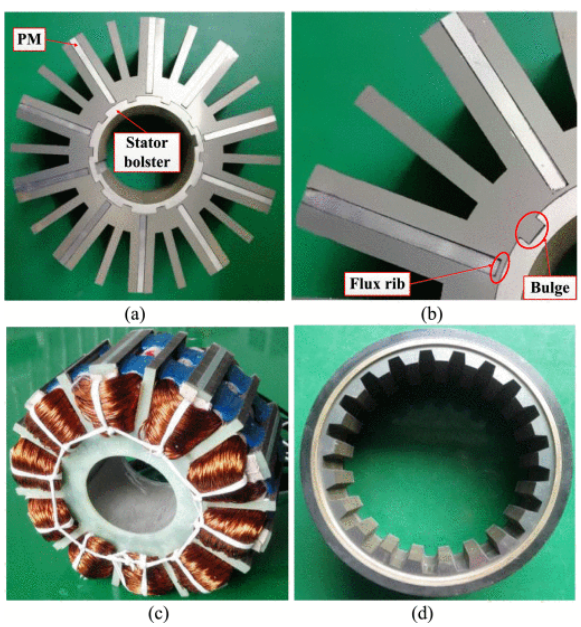

Fig. 4. Prototype of the five-phase FSPM machine. (a) Stator. (b) Zoom in of the stator. (c) Wound stator. (d) Rotor.

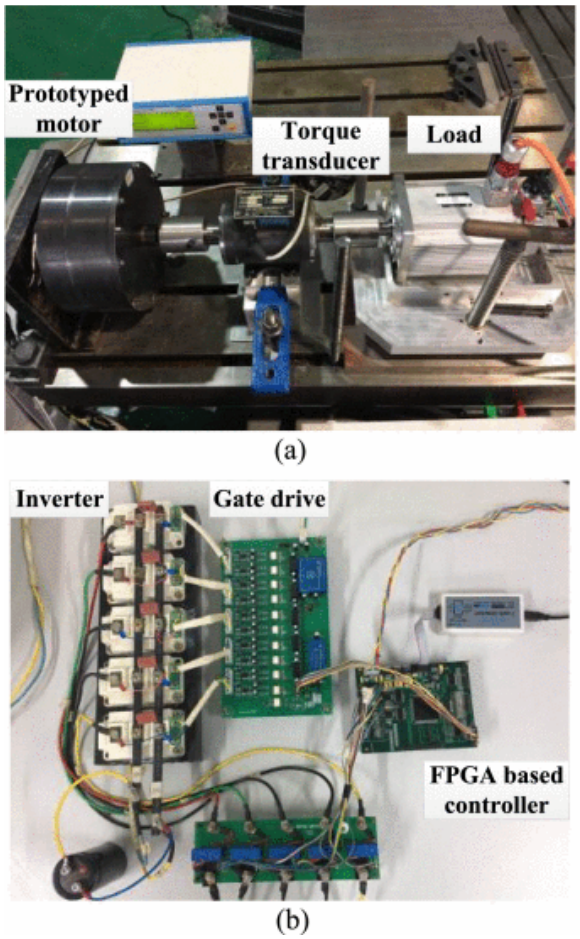

Fig. 5. (a) Test hardware setup. (b) Five-phase inverter.

The phase back-EMF waveforms and the torque profiles of the prototyped motor from simulation (including 2-D and 3-D FEA predictions) and experiment, are shown in Fig. 6 and Fig. 7, respectively. As can be seen, the results from CE-FEA (2-D) and TS-FEA (2-D) for both the back-EMF waveforms and the torque profiles, are in very good agreement. There are discrepancies of about 6.5% and 7.2% for the fundamental component amplitude of back-EMF and the average torque, respectively, between the CE-FEA and TS-FEA (3-D) results, mainly due to end-effects. In addition, there are discrepancies of about 3.3% and 6.0% for back-EMF and average torque, respectively, between the TS-FEA (3-D) and experimental results, due to the imperfections of manufacturing and assembling processes, material properties variations, as well as measurement inaccuracies. Overall, it is fair to state that the results from TS-FEA (2-D and 3-D) and experiment have verified the validity and accuracy of the CE-FEA. Consequently, the CE-FEA is a reliable approach to be used throughout the following large-scale optimization.

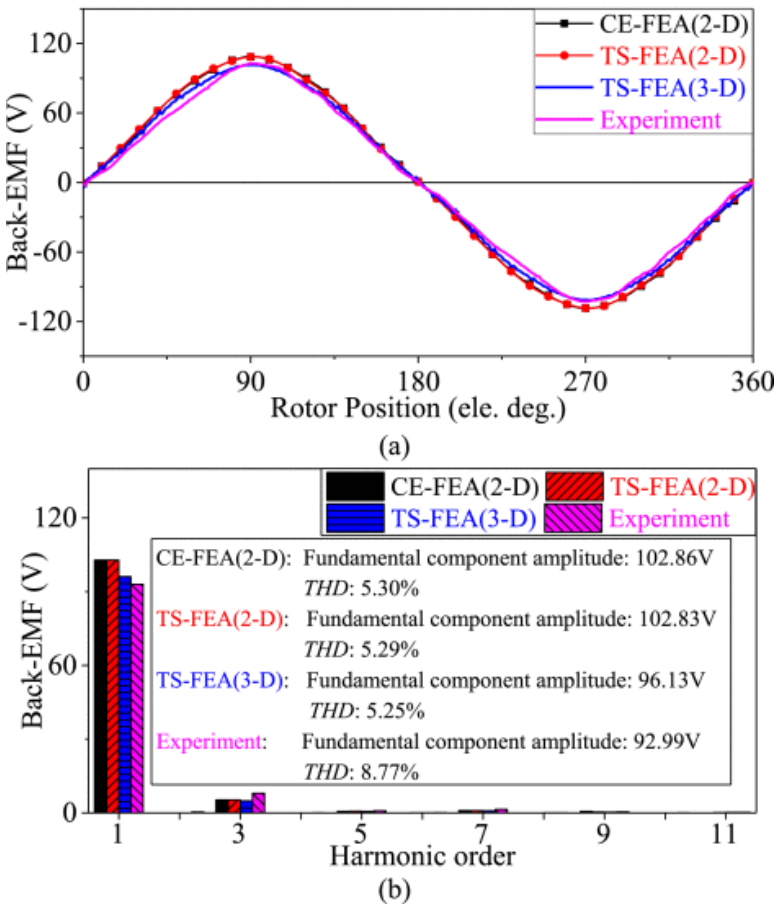

Fig. 6. (a) FEA-predicted and measured back-EMF of the FSPM machine @ 500 r/min. (b) Harmonic Spectrum.

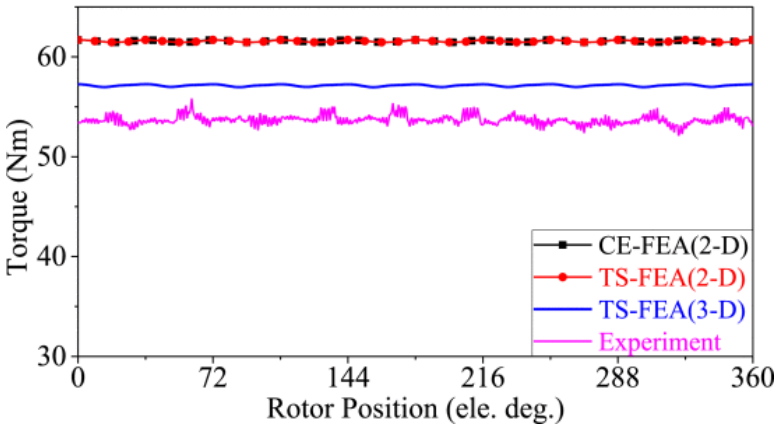

Fig. 7. FEA-predicted and measured torque profiles at the rated condition.

SECTION III. Design Techniques for Driving Cycles

A driving cycle is a signature of driving characteristics of a zone in the time-domain consisting of several vehicle operations, such as acceleration, deceleration, idling, and cruising, targeting a more accurate description of the actual vehicle operating conditions.

A. Specification of the Investigated Driving Cycles

Three typical driving cycles are considered in this paper. First, the Urban Dynamometer Driving Schedule (UDDS), as reported in Fig. 8(a), is suitable for city driving. It represents an urban route with frequent stops and most of its energy is consumed in the relatively low-speed region. Second, the Highway Fuel Economy Driving Schedule (HWFET), as reported in Fig. 8(b), stands for highway driving. It is characterized by a non-stop operation and a large part of its energy consumption occurs in the relatively high-speed region. The third one is a combined UDDS/HWFET driving cycle, which means one HWFET driving cycle after one UDDS cycle, as reported in Fig. 8(c).

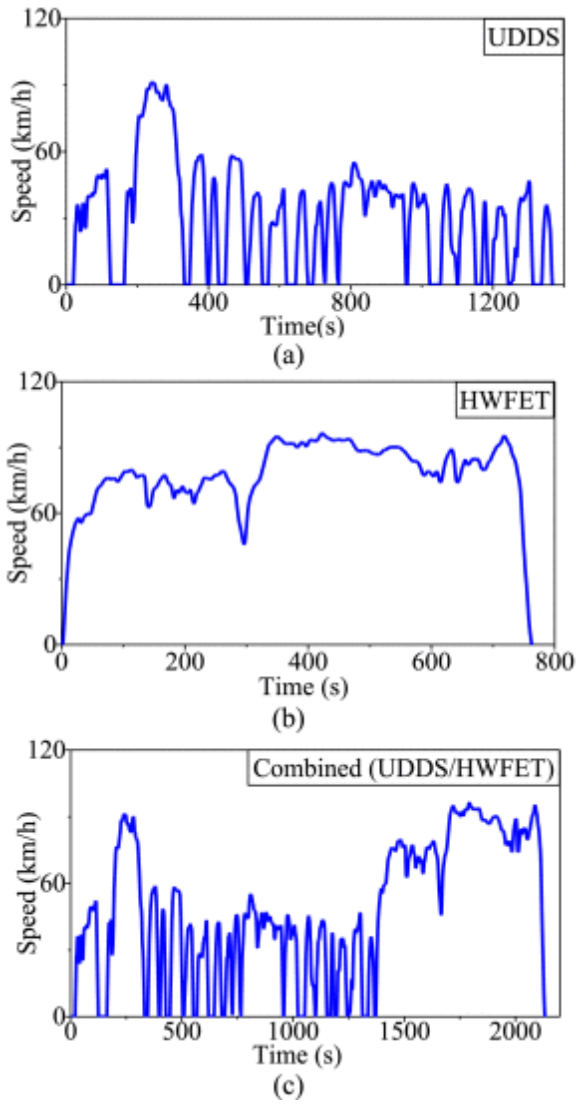

Fig. 8. Driving cycle speed profiles. (a) UDDS. (b) HWFET. (c) Combined UDDS/HWFET.

The investigated vehicle is a micro-sized direct-drive car with a distributed drivetrain, which employs four in-wheel FSPM machines. The specifications of the vehicle are listed in Table III. Based on the driving cycle speed profiles shown in Fig. 8 and the vehicle specifications listed in Table III, the required motor torque profiles are calculated by using the vehicle dynamics model in ref. [20], as shown in Fig. 9. The torque is calculated using eq. (4) on the basis of the traction force, F_t, which is computed from the inertia force F_a, rolling force, F_r, and drag force F_d.

$$\left.\begin{aligned} F_a &= m \cdot a \\ F_r &= k_r \cdot m \cdot g \\ F_d &= \frac{1}{2} \cdot \rho \cdot c_d \cdot S \cdot v^2 \\ F_t &= F_a + F_r + F_d \end{aligned}\right\} \quad (4)$$

where, m is the vehicle mass, a and g are the vehicle and gravitational acceleration, c_r is the rolling resistance coefficient, ρ is the air density, c_d is the drag coefficient, S is the frontal area, v is the vehicle speed. It should be noted that the vehicle dynamics model is performed on a flat route. Since the machine is designed for motor application, the regenerative area is not taken into account in this analysis.

TABLE III Specifications of the Investigated Vehicle

Parameter	**Value**
Vehicle mass (kg)	500
Radius of wheels (m)	0.258
Frontal area (m^2)	0.6
Rolling resistance coefficient	0.0054
Air density (kg/m^3)	1.25
Drag coefficient	0.26
Gravitational acceleration (m/s^2)	9.8

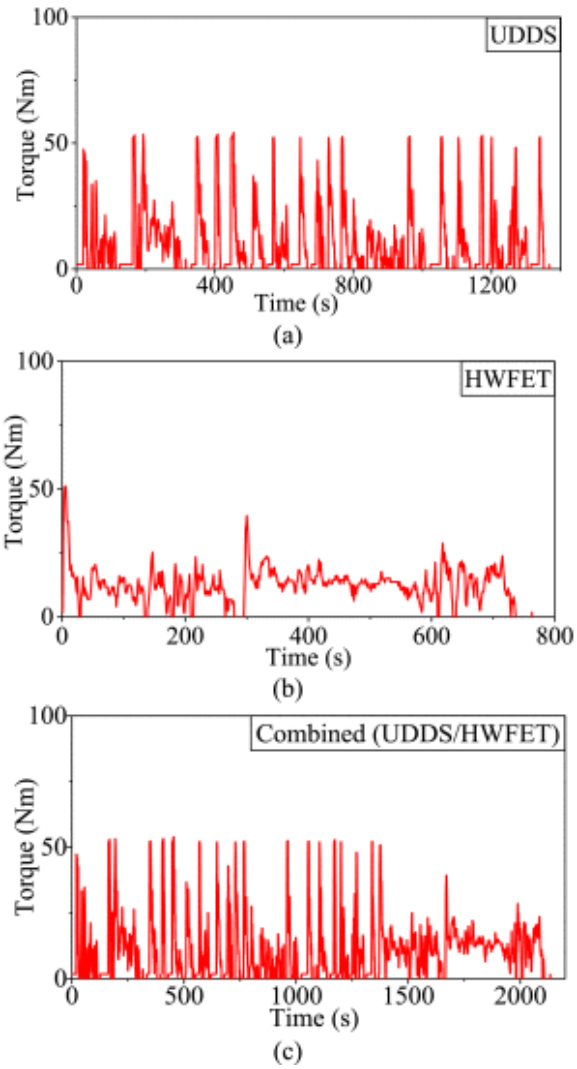

Fig. 9. Driving cycle torque profiles. (a) UDDS. (b) HWFET. (c) Combined UDDS/HWFET.

B. Representative Operating Points Extraction

It is well-known that the operating points are very dynamic and widely distributed in the torque-speed plane. It is practically impossible to optimize the motor with consideration of the whole operating points. Hence, the technique of representative points is implemented to equivalently model the specific driving cycle by a finite number of points as follows. First, the machine energy consumption of every single operating point in the driving cycle is calculated according to the torque and speed fluctuations. Then, the points are partitioned into several clusters by the *k*-means clustering algorithm as shown in Fig. 10(a), (b), and (c), respectively. *k*-means algorithm is a cluster analysis in data mining, which partitions the points into *k* clusters [21]. The clustering algorithm mainly includes two steps:

1. Each candidate, x_p, is initially assigned to the cluster, S_i, by eq. (5).

$$S_i^{(t)} = \{x_p \| \|x_p - m_i^{(t)}\|^2 \leq \|x_p - m_j^{(t)}\|^2\}, \quad j = 1,2,\dots k \tag{5}$$

where, t is the iteration number. m_i is the nearest mean of the cluster, S_i. For the initial iteration, $m_i^{(0)}$ is chosen randomly.

1. The centroids of the candidates in the new clusters, $m_{(t+1)i}$, according to eq. (6), are designated as the updated means.

$$m_i^{(t+1)} = \frac{1}{|S_i^{(t)}|} \sum_{x_j \in S_i^{(t)}} x_j \qquad (6)$$

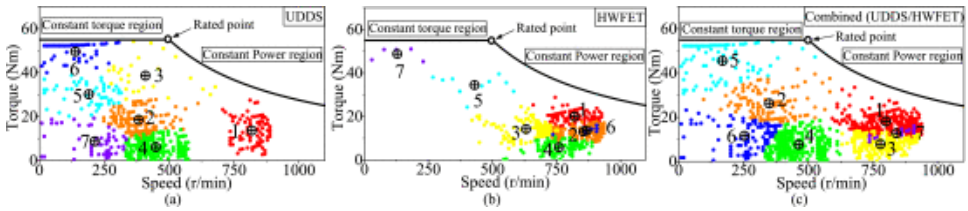

Fig. 10. Respective points and clusters obtained by *k*-means algorithm of the three driving cycles. (a) UDDS. (b) HWFET. (c) Combined (UDDS/HWFET).

The assignment in step 1 and the update in step 2, are iteratively repeated until the $m_i^{(t)}$ does not change. Finally, the energy centroids of the clusters are extracted as representative points, while the energy weight, w_i, means the energy of its associated cluster as a percentage of the total energy consumption, as listed in Table IV.

TABLE IV Representative Points of the Three Driving Cycles

	UDDS			**HWFET**			**Combined (UDDS/HWFET)**		
Representative points	n **(r/min)**	T_{avg} **(Nm)**	w_i	n **(r/min)**	T_{avg} **(Nm)**	w_i	n **(r/min)**	T_{avg} **(Nm)**	w_i
1	818	14	0.274	820	20	0.338	799	18	0.439
2	383	19	0.247	855	13	0.270	348	26	0.151
3	408	39	0.133	631	14	0.218	778	8	0.142
4	449	6	0.131	759	6	0.101	463	8	0.107
5	190	30	0.096	430	34	0.040	169	46	0.095
6	138	50	0.092	868	14	0.025	253	12	0.039
7	213	9	0.027	128	49	0.008	839	13	0.027

It should be noted that the number of clusters, *k*, is determined based on the sum of the distances of the load points to their corresponding cluster means as shown in Fig. 11. The sum of the distances is defined as,

$$Sum of the distances = \sum_{i=1}^{k} \sum_{x_j \in S_i^{(t)}} \|x_j - m_i\|^2 \qquad (7)$$

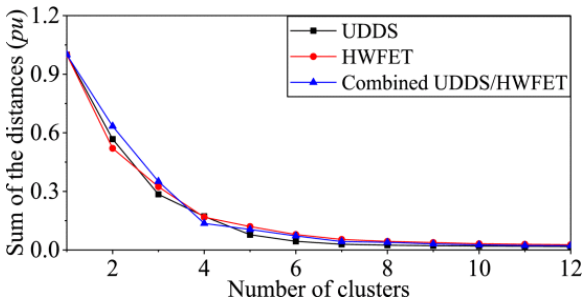

Fig. 11. The accuracy of the driving cycle modeling versus number of clusters.

The fact that the "*Sum of the distances*" is normalized by dividing its value at the number of clusters equal to 1 in Fig. 11, should be noted. As observed, 7 clusters are a good compromise between accuracy and computational cost. A larger number of clusters would not provide more meaningful accuracy but suffer from more computational cost.

For comparative purposes, the ideal rated/base point (55 Nm at 500 r/min) is highlighted in Fig. 10, assuming a hyperbolic trend in the extended speed region. As can be seen, the majority of the operating points are covered by the continuous torque-speed envelope. This implies that the motor can run over the three driving cycles within its thermal limits. The performance rates are typical for a light-duty vehicle.

C. Armature Current Calculation for the Representative Points

In order to evaluate the electromagnetic performance of a candidate design at a specific torque and speed, the armature current should be accurately calculated for each representative point. The linear flux linkage-based model fails to predict the electromagnetic performance due to the high-level saturation in FSPM machines, while sweeping the whole $i_d - i_q$ plane will be much time-consuming [22]. To reduce the computational burden as much as possible without loss of accuracy, the method of response surface methodology (RSM) [23] combined with CE-FEA is utilized to obtain the inverse machine model as follows with a design as an example:

1. The central composite design (CCD) method as one of design of experiments (DOE) techniques is implemented to generate as few as 9 experiments, while the *d*- and *q*-axis flux linkage, λ_d and λ_q, are calculated by CE-FEA as listed in Table V, where, c_i is the coded design variable which is defined as:

$$c_i = [x_i - (x_{i\_max} + x_{i\_min})/2] / [(x_{i\_max} + x_{i\_min})/2], i = 1,2. \quad (8)$$

TABLE V Designs Generated by the CCD Method

Exp.	c_1	c_2	λ_d (Wb)	λ_q (Wb)
1	-1.414	0	0.0845	0.0116
2	0	0	0.0561	0.0450
3	1.414	0	0.0199	0.0826
4	1	-1	0.0697	0.0848
5	0	-1.414	0.0899	0.0542
6	-1	-1	0.0879	0.0259
7	-1	1	0.0702	0.0094
8	1	1	0.0020	0.0344
9	0	1.414	0.0360	0.0087

where, x_1, x_2 are the phase current and the current vector angle, respectively.

1. The λ_d and λ_q, as functions of c_1 and c_2 are modeled by a second-order polynomial function, respectively, which is formulated as:

$$y = \beta_0 + \sum_{i=1}^{2} \beta_i c_i + \sum_{i=1}^{2} \beta_{ii} c_i^2 + \beta_{12} c_1 c_2 \qquad (9)$$

where, y is the dependent variable, here it is the flux linkage, while β_0 , β_iβi , β_{ii} , and $\beta_{12}$are the regression coefficients. Based on eq. (9), the RSM model of λ_d and λ_q, is constructed as shown in Fig. 12. To verify the accuracy of the CCD and RSM methods, six standard FEA simulations with different armature currents are conducted as listed in Table VI. It should be noted that the selected six simulations are different with the 9 experiments in Table V, where, I is the phase current, γ is the current vector angle (the current advanced angle with respect to the q-axis). As can be seen, the results from the constructed RSM and standard FEA simulations are in good agreement. Therefore, the CCD method and the RSM model is reliable for FEA approximation.

1. For each representative point with a specific torque and speed, the armature current is calculated such that: If the speed ω < the base speed ω_{base}, the motor operates in the maximum torque-per-ampere mode, the armature current (I and γ) is the solution of the torque equation, eq. (10), with minimum current amplitude. Where, N_r is the number of rotor teeth, I_d and I_q are the *d*- and *q*-axis currents, respectively; If $\omega \geq \omega_{base}$, the motor is controlled by the flux-weakening mode, the armature current is the solution of eq. (10), not only with minimum current amplitude, but also in the condition that its voltage is below or equal to the rated voltage [15]. The voltage is expressed by eq. (11). It should be noted that the *d*- and *q*-axis flux linkage, $\lambda_d(I,\gamma)$ and $\lambda_q(I,\gamma)$, come from the RSM model in Fig. 12 by look-up tables.

$$\begin{aligned} T(I,\gamma) &= \frac{5}{2} N_r [\lambda_d(I,\gamma) \times I_q - \lambda_q(I,\gamma) \times I_d] \\ &= \frac{5}{2} N_r [\lambda_d(I,\gamma) \times I \cdot \cos(\gamma) - \lambda_q(I,\gamma) \\ &\quad \times I \cdot \sin(\gamma)] \\ V(I,\gamma) &= \omega_e \sqrt{\lambda_d(I,\gamma)^2 + \lambda_q(I,\gamma)^2} \end{aligned} \qquad (10)(11)$$

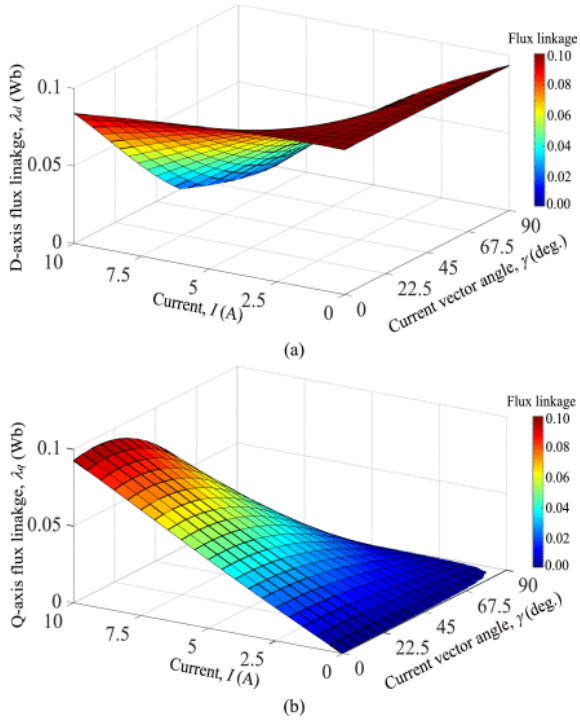

Fig. 12. RSM model for flux linkage. (a) D-axis flux linkage. (b) Q-axis flux linkage.

TABLE VI. Comparison of Results From RSM Model and FEA Simulations

			λ_d (Wb)		λ_q (Wb)	
No.	***I***	***γ***	**RSM**	**FEA**	**RSM**	**FEA**
1	2.0	10	0.09057	0.09058	0.01698	.01696
2	2.0	50	0.08145	0.08144	0.01133	0.01131
3	5.0	20	0.07729	0.07731	0.04277	0.04378
4	5.0	60	0.05398	0.05399	0.02478	0.02479
5	8.0	30	0.05190	0.05194	0.06985	0.06989
6	8.0	70	0.01474	0.01476	0.02999	0.02996

SECTION IV. Optimization Strategy

The optimization process of the five-phase FSPM machine is illustrated in this section, including four case-studies, i.e., (1) traditional optimization at the rated operating point, and optimizations for specific driving cycles as depicted in Section III above, namely, (2) UDDS, (3) HWFET, (4) Combined UDDS/HWFET.

A. Parametrization of the FSPM Machine Model

The five-phase outer-rotor FSPM machine is parameterized as shown in Fig. 13. There are ten independent design variables which are defined by ratio expressions in order to avoid the geometrical conflicts in the automated optimization procedure as listed in Table VII, where, R_{ro}, R_{ri}, R_{so}, and R_{si} are the outer and inner radii of the rotor and stator, respectively, h_g is the radial air-gap height, τ_r and τ_s are the rotor and stator pole pitches in degrees, β_t is the rotor pole-arc width in degrees, β_b is the rotor pole-arc width at its inner yoke radius, h_r, h_{sy}, and l_{pm} are the heights of the rotor tooth, the stator yoke, and the PM, respectively, while α_{pm} is the PM-arc width, α_f and α_t are the fault-tolerant tooth and stator tooth arc width.

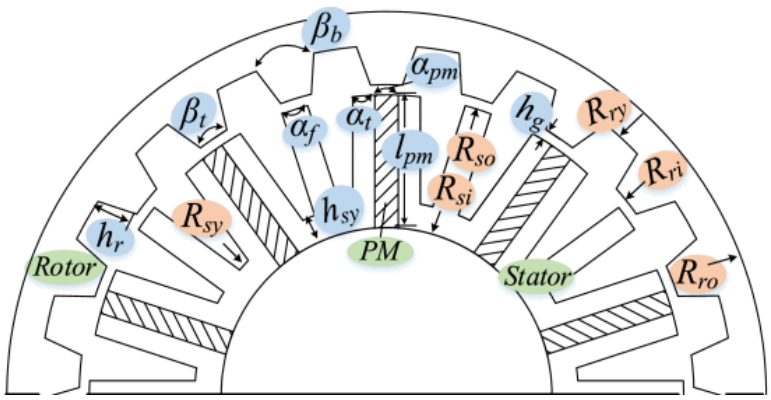

Fig. 13. Parametric model of the five-phase FSPM machine.

TABLE VII Design Variables and Their Bounds

Variables	Definition	Min	Max
k_{si}	R_{ri}/R_{ro}	0.7	0.85
h_g	Fig. 13	0.5 mm	1.2 mm
k_r	β_t/τ_r	0.15	0.5
k_{ry}	β_b/τ_r	0.15	0.8
k_{hr}	$h_r/(R_{ro}-R_{ri})$	0.3	0.7
k_{pm}	α_{pm}/τ_s	0.05	0.15
k_{lpm}	l_{pm}/R_{so}	0.3	0.6
k_{st}	α_t/τ_s	0.1	0.2
k_{ft}	α_f/τ_s	0.1	0.2
k_{sy}	$h_{sy}/(R_{so}-R_{si})$	0.16	0.4

B. Optimization Fitness Function

A robust population-based metaheuristic optimization algorithm, namely Differential Evolution (DE), is utilized to identify the superior designs and converge towards the optimal region in the large-scale design space. The DE algorithm includes mutation and crossover operations which mimics the Darwinian evolution as presented in [24], [25].

Two objectives are considered in the four optimization case-studies, respectively:

- Minimizing the stack length to maximize the torque density;
- For the first case-study (traditional optimization against rated point), maximize the efficiency, η, at the rated operating point:

$$\begin{aligned} \eta &= [P_{out}/(P_{out}+P_{loss})] \times 100\% \\ P_{loss} &= P_{Cu}+P_{Fe}+P_{eddy} \end{aligned} \quad (12)(13)$$

where, P_{out} is the output power, P_{Cu}, P_{Fe}, and P_{eddy} are the losses of copper, iron core, and eddy-current in PMs, respectively. It should be noted that P_{Cu} is calculated by a strand eddy-current loss model in ref. [26] with the aim to include the skin-effect and strand eddy-current losses due to the presence of slot leakage and fringing fluxes. While P_{Fe} and P_{eddy} are calculated with the core losses and magnet losses models in ref. [27]and [28]. It should be noted that the harmonic effect of the switching supply is neglected. The designs are considered at the temperature of 95 °C with a typical oil-forced cooling system, which is based on previous experience with the same current density. Transient thermal analysis of the machine is not directly addressed at this stage of research and will be investigated in a future work.

For the other three case-studies (optimization targeting the whole driving cycles), maximize the cycle energy efficiency:

$$\eta_{cycle} = \frac{\sum_i (P_{out,i} \cdot w_i)}{\sum_i [(P_{out,i} + P_{loss,i}) \cdot w_i]} \qquad (14)$$

Meanwhile, the torque ripple and flux-weakening capability are defined as constraints:

- For the first case-study, the torque ripple under the rated load condition, $T_{rip} \leq 20\%$, while for the other three case-studies, the torque ripple at each representative point, $T_{rip,i} \leq 30\%$;
- The flux weakening capability, $k_{fw} = \lambda_m / (\lambda_m - L_d I_{rated}) \geq 2$;

where, λ_m is the PM flux linkage, L_d is the *d*-axis inductance, I_{rated} is the rated current.

It should be noted that throughout the optimization process, the outer diameter of each candidate design is fixed, while the stack length is scaled to obtain the rated power rating of 55 Nm at 500 r/min. The overall automated optimization procedure is schematically represented in Fig. 14. It was implemented by MATLAB scripting and ANSYS/Maxwell simulation. ANSYS is used for FE solutions of the candidate design. While the post-processing of the data obtained from ANSYS, as well as the DE algorithm are performed in MATLAB. The data exchange between MATLAB scripting and ANSYS/Maxwell simulation is shown in Fig. 15. For the first generation, the performance of each candidate design is evaluated with the CE-FEA technique. Then, these candidate designs are compared with each other. Some of them are selected by DE algorithm to get into next generation. The procedure above will be repeated until the termination criteria is satisfied. It should be noted that there are two steps with CE-FEA. The first one is used for determination of the stack length and the number of turns for each candidate design, as well as for setting up experiments in CCD (See Table V) to calculate the *d*- and *q*-axis flux linkage, λ_d and λ_q. The stack length, L_{sk}, is determined by,

$$L_{sk} = L_{sk\_0} \cdot \frac{55}{T} \qquad (15)$$

where, $L_{sk_0}$is the original stack length, *T* is the output torque calculated when the rated phase current of 10 A is applied. The number of turns, *NC*, is determined by,

$$NC = \mathrm{nint}\left(\frac{A_s \cdot S_f \cdot C_d \cdot 10^6}{I_{rated}}\right) \qquad (16)$$

where, "nint" is a function which returns the nearest integer, A_s is the area of the slot, S_f is the slot fill factor, C_d is the current density. It should be noted that for all of the candidate designs, the slot fill factor, S_f, and the current density, C_d, are fixed as 45% and 4 A/mm^2, respectively. The second "CE-FEA" in Fig. 14 is used for computing the motor's electromagnetic characteristics with the armature current determined from the flux linkage surface.

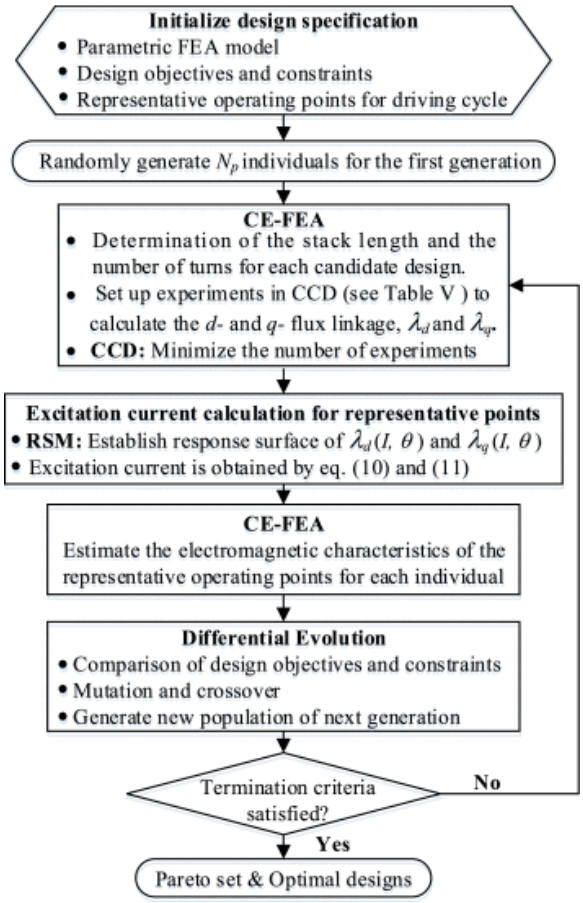

Fig. 14. Flowchart of the automated optimization targeting driving cycles.

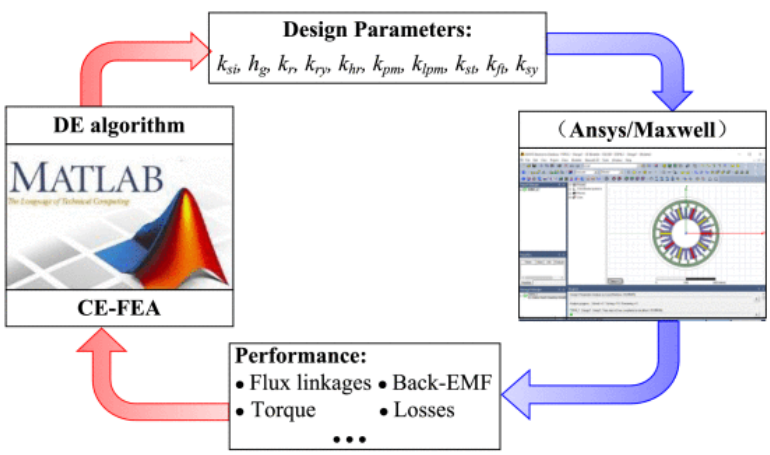

Fig. 15. Data exchange between MATLAB and ANSYS/Maxwell simulation.

C. Optimization Results

The optimization results of the motor design under different operating conditions are depicted in Fig. 16(a), (b), (c), and (d), respectively, which were obtained by employing 200 generations in the DE algorithm, each generation containing 50 designs, thus yielding a total number of 10,000 candidate designs for each large-scale optimization problem. In Fig. 16, the blue circles stand for the members of initial iterations while the red circles stand for those in the final iterations. As can be seen, with the number of iterations increasing, the candidate designs evolve toward the Pareto front, where the designs are of relatively low stack

length and high efficiency/cycle energy efficiency. These results verify the validity of the proposed optimization strategy in achieving the desired outcomes in this paper. In addition, the scatter plots in Fig. 16 show that the two objectives considered in these case-studies, namely, short stack length and high efficiency/cycle energy efficiency, are conflicting. Therefore, there is no one best design, but rather a family of “best compromise” designs along the Pareto front, for which any improvement in one objective will lead to a deterioration in the other objective. These four Pareto fronts are delineated clearly in Fig. 16(a), (b), (c), and (d), respectively.

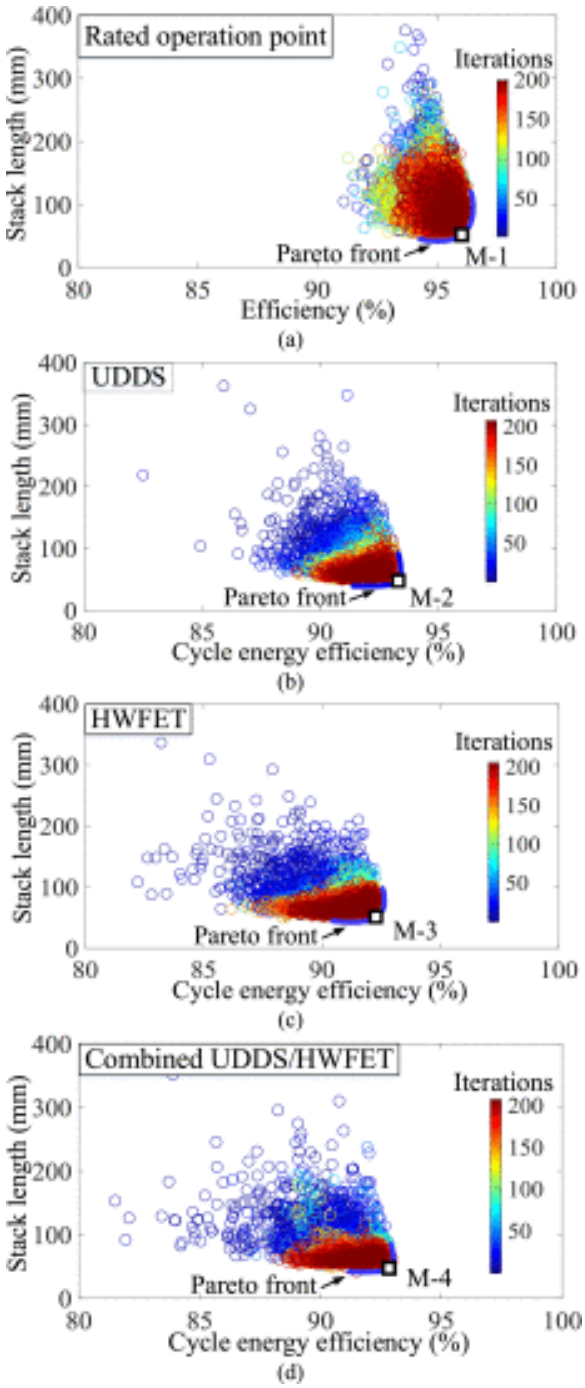

Fig. 16. Scatter plot and Pareto sets for DE optimization of the motor under different operating conditions. (a) Optimization against the rated point. (b) UDDS. (c) HWFET. (d) Combined UDDS/HWFET.

SECTION V. Comparison and Discussion

Based on the Pareto fronts in Fig. 16(a), (b), (c), and (d), four optimal designs denoted by M-1, M-2, M-3 and M-4, respectively, are selected for the rated operating point, the UDDS, the HWFET, and the combined UDDS/HWFET driving cycles, respectively. As mentioned in Section IV, part *C*, there is no one best design for multi-objective optimization, while the designs which are along the Pareto front are the "best compromise" designs. These four designs are selected because they are along the Pareto front and located on the corner of each Pareto front. It indicates that these four selected optimal designs are the "best compromise" designs for the two objectives in each optimization results. Their cross-sections are shown in Fig. 17(a), (b), (c), and (d), respectively. Their main parameters and performance characteristics are listed in Table VIII. It should be noted that the material cost of the four optimal designs is also provided in this table. The material cost is calculated by,

$$\text{Cost} = 24 \cdot m_{PM} + 3 \cdot m_{Cu} + 1 \cdot m_{Fe} \qquad (17)$$

where, m_{PM}, m_{Cu}, and m_{Fe} are the masses of the PM, copper wires, and the ferromagnetic sheets of the rotor and stator, respectively.

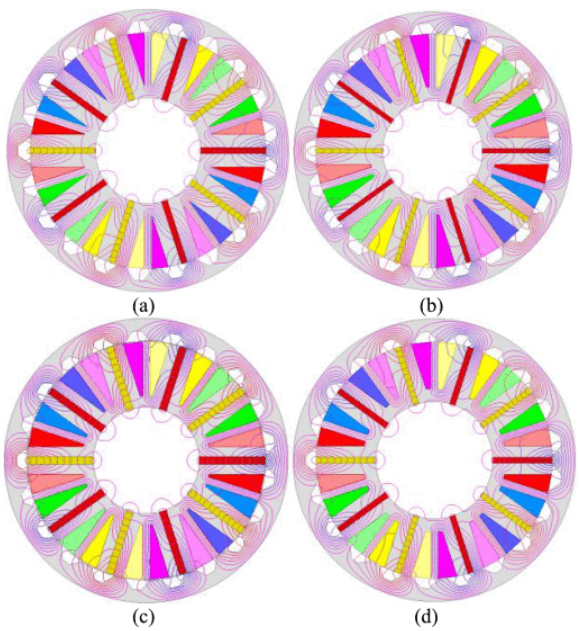

Fig. 17. Cross-sections of the selected optimal designs. (a) M-1. (b) M-2. (c) M-3. (d) M-4.

TABLE VIII. Main Parameters and Performance of the Four Optimal Designs

Items	**M-1**	**M-2**	**M-3**	**M-4**
	(Rated point	**(UDDS)**	**(HWFET)**	**(UDDS/HWFET)**
Geometrical parameters				
k_{si}	0.841	0.843	0.846	0.845
h_g (mm)	0.60	0.75	1.13	0.88
k_r	0.254	0.247	0.326	0.277
k_{ry}	0.753	0.586	0.756	0.791
k_{hr}	0.516	0.379	0.429	0.413
k_{pm}	0.080	0.062	0.096	0.076
k_{lpm}	0.552	0.570	0.552	0.505
k_{st}	0.181	0.176	0.140	0.152
k_{ft}	0.102	0.106	0.101	0.103

k_{sy}	0.199	0.243	0.171	0.218
R_{si} (mm)	42.13	40.41	42.11	41.16
a_{pm} (deg.)	2.89	2.24	3.44	2.74
l_{pm} (mm)	51.88	53.62	51.95	53.00
Stack length (mm)	58.24	56.61	59.70	57.87
Number of turns/phase	104	114	134	126
Electrical performance				
Phase resistance (Ω)	0.125	0.133	0.162	0.154
Shaft torque (Rated) (Nm)	55	55	55	55
Torque ripple (Rated) (%)	1.74	2.27	0.60	2.32
η (Rated point) (%)	**95.75**	95.24	94.99	95.15
η_{cycle} (UDDS) (%)	92.44	**93.12**	92.31	92.87
η_{cycle} (HWFET) (%)	90.60	90.86	**92.11**	91.46
η_{cycle} (Combined) (%)	91.34	91.21	92.04	**92.46**
Cost	41.44	36.09	48.41	38.27

As can be seen, the variation of the stack length of the four optimal machine designs is less than 3% from each other, which means that the torque densities of the four machines are almost the same. It is also interesting to note that the geometric parameters of the M-2 design are much closer to those of the M-1 design, while those of the M-4 design tend to be a balance/compromise between the M-2 design and the M-3 design. This will be further explained in the following part. The main purpose of this paper is to optimize the efficiency according to the specific operating conditions (driving cycles) of the motor in order to reduce energy consumption as much as possible. Therefore, the efficiency and cycle energy efficiencies of the four machine designs at the rated operating point, the UDDS, the HWFET, and the combined UDDS/HWFET driving cycles were calculated and compared in Table VIII. The results were obtained by running each machine design under the four different operating conditions. It is clearly observed that among the four optimal machine designs, the efficiency at the rated operating point of the M-1 design is the highest. By contrast, the M-2 design, which was optimized versus the UDDS driving cycle, outperforms the other three in terms of cycle energy efficiency over this UDDS driving cycle, because special attention has been paid to minimize the losses over its corresponding representative points during the optimization process. So do the M-3 design for the HWFET driving cycle and the M-4 design for the combined UDDS/HWFET driving cycle, respectively. The above indicates that the sought purpose is achieved by the proposed optimization strategy in this paper. It should be noted that even though the difference of efficiency/cycle energy efficiency of the four selected designs is not quite large, an increment of only 0.5% in efficiency/cycle energy efficiency can bring very significant reduction of energy consumption, which is of paramount importance.

A breakdown of the loss components will benefit one in understanding of the influence of the optimization strategies on the design outcomes. Therefore, the loss components of the four optimal designs over the four different operating conditions were calculated and depicted in Fig. 18(a), (b), (c), and (d), respectively. Without loss of generality, the weighted losses were calculated for the driving cycle cases. For example, the weighted copper losses, P'_{Cu}, are calculated by,

$$P'_{Cu} = \sum_i (P_{Cu,i} \cdot w_i) \qquad (18)$$

where, $P_{Cu,i}$ is the copper losses at the *i*th representative operating point in the specific driving cycle. The weighted PM eddy-current losses, P'_{eddy}, and the weighted core losses, P'_{Fe}, are obtained by the same method as the weighted copper losses, P'_{Cu}.

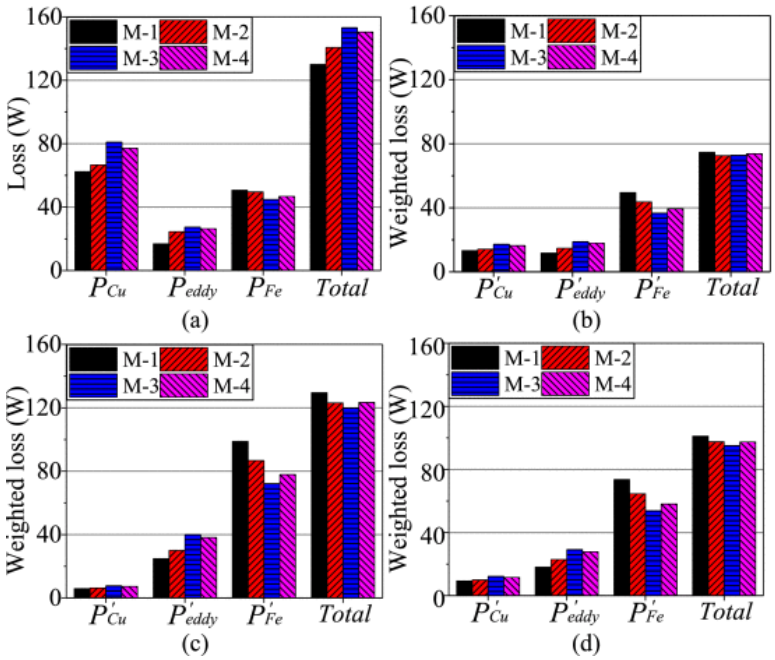

Fig. 18. Loss components. (a) At the rated operating point. (b) UDDS driving cycle. (c) HWFET driving cycle. (d) Combined UDDS/HEFET driving cycle.

As can be seen from Fig. 18(a), since copper losses are dominant at the rated operating point, and the copper loss of the M-1 design is the lowest, it follows that the efficiency of the M-1 design at rated point is the highest. Also, it is interesting to note that the resistance and the number of turns per phase of the M-1 design are the lowest, while the output torques of the four motors are the same. Therefore, the magnetic loading of the M-1 design will be the highest, furthermore, the saturation is the most serious and it turns out to have high core losses. From Fig. 18(b), the total losses of the M-2 design are the lowest because its copper losses and PM eddy-current losses are relatively low even though its core losses are relatively high. From Fig. 18(c), in the case of the HWFET driving cycle attention is paid more on the performance in the high-speed region, where the core losses are dominant. As expected, the core losses of the M-3 design are the lowest and its efficiency is the highest. While for all the operating conditions, the M-4 design, which is optimized versus the combined UDDS/HWFET driving cycle, tends to be a compromise result among the three loss components. The result is consistent with the data in Table VIII.

To further clarify the tradeoff of the optimization for the four operating conditions, the efficiency maps overlaid with their corresponding representative points (Table IV) of the four optimal designs are depicted in Fig. 19(a), (b), (c), and (d), respectively. As can be seen, the M-1 design is obtained from the optimization at the rated operating point, which is 55 Nm at 500 r/min, that is located in high-efficiency area in Fig. 19(a). Meanwhile, since the UDDS driving cycle is relatively concentrated in the low-speed region, the high-efficiency area of the M-2 design is closer to the low-speed region as shown in Fig. 19(b). Similarly, the HWFET operation is concentrated in the high-speed region. Thus, the optimization is achieved by extending the high-efficiency area to the high-speed low-torque region as shown in Fig. 19(c). Meanwhile, the efficiency map of the M-4 design tends to be a compromise between those of the M-2 design and the M-3 design as shown in Fig. 19(d).

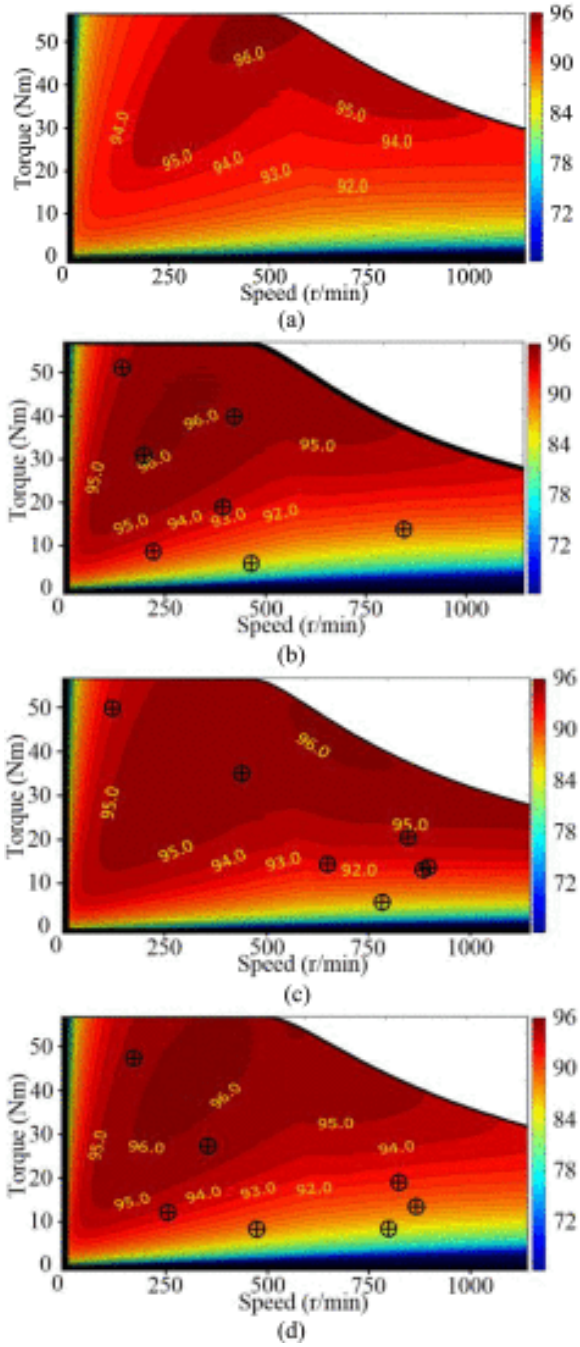

Fig. 19. Efficiency maps. (a) M-1. (b) M-2. (c) M-3. (d) M-4.

Based on the efficiency maps in Fig. 19, the energy consumptions over all the operating points of the driving cycle in Fig. 10 (color-coded points) are compared with those calculated by using the representative points. The results are listed in Table IX.

TABLE IX. Energy Consumption Comparison

	M-2	**M-3**	**M-4**
	(UDDS)	**(HWFET)**	**(UDDS/HWFET)**
Energy over all points (kJ)	353.93	415.88	776.23
Energy over the representative points (kJ)	359.74	424.09	785.20
Percentage difference (%)	1.6%	1.9%	1.1%

As can be observed, the percentage difference of the energy consumptions calculated by the two different methods for the three driving cycles are within 2% of each other. This indicates that the representative operating points listed in Table IV provided a good representation of the overall operating points for the three driving cycles.

SECTION VI. Conclusion

An application-oriented design optimization method for a five-phase FSPM machine is introduced in this paper. The influence of different operating conditions on the optimization results is investigated and compared, including the traditional optimization performed at the rated operating point, and the optimization targeting the whole driving cycles (the UDDS, the HWFET, and the combined UDDS/HWFET, representing the city, highway, and combined city/highway driving conditions, respectively). The following conclusions can be drawn as:

To reduce the computational burden, three techniques are implemented: 1) The CE-FEA instead of TS-FEA is utilized to evaluate the electromagnetic performance of the five-phase FSPM machine. The accuracy and reliability of the CE-FEA are verified by experimental results; 2) Representative operating points are extracted by the *k*-means clustering algorithm; 3) An inverse motor model is constructed by the RSM method to calculate the armature current at each representative point. With the benefits of these techniques, significant reduction of the execution time is achieved (at least two orders of magnitude). This enables a comprehensive search algorithm in wide design ranges for large-scale optimization in a practical engineering environment.

Comparing the four optimal designs under different operating conditions, it has been shown that the optimal designs are dependent on the characteristics of the operating conditions/driving cycles in terms of geometry, efficiency, and energy loss distributions. For the traditional optimization performed at the rated operating point, the optimal design tends to reduce copper losses but suffer from high core losses; For UDDS, the optimal design tends to minimize both copper losses and PM eddy-current losses in the low-speed region; For HWFET, the optimal design tends to minimize core losses in the high-speed region; For the combined UDDS/HWFET, the optimal design tends to balance/compromise the loss components in both the low-speed and high-speed regions.

The results and conclusions provide guidance to the designers/engineers that if the motor is used in a car which usually runs in the city driving condition, the optimal design from the optimization targeting the UDDS driving cycle instead of the traditional optimization performed at the rated operating point, will be preferable. So do the optimal designs for the highway and combined city/highway driving conditions from the optimization targeting the HWFET and the combined UDDS/HWFET driving cycles, respectively. Therefore, the optimization of the motor design with concrete and solid analysis for specific driving conditions/cycles is feasible and practical.

ACKNOWLEDGMENT

The authors would like to thank the software support of ANSYS, Inc.

REFERENCES

1. M. Zeraoulia, M. E. H. Benbouzid, D. Diallo, "Electric motor drive selection issues for HEV propulsion systems: A comparative study", *IEEE Trans. Veh. Technol.*, vol. 55, no. 6, pp. 1756-1764, Nov. 2006.

2. J. Lin, N. Schofield, A. Emadi, "External-rotor 6–10 switched reluctance motor for an electric bicycle", *IEEE Trans. Transp. Electrific.*, vol. 1, no. 4, pp. 348-356, Dec. 2015.

3. M. Terashima, T. Ashikaga, T. Mizuno, K. Natori, N. Fujiwara, M. Yada, "Novel motors and controllers for high-performance electric vehicle with four in-wheel motors", *IEEE Trans. Ind. Electron.*, vol. 44, no. 1, pp. 28-38, Feb. 1997.

4. Y. Shi, L. Jian, J. Wei, Z. Shao, W. Li, C. C. Chan, "A new perspective on the operating principle of flux-switching permanent-magnet machines", *IEEE Trans. Ind. Electron.*, vol. 63, no. 3, pp. 1425-1437, Mar. 2016.
5. B. L. J. Gysen, E. Ilhan, K. J. Meessen, J. J. H. Paulides, E. A. Lomonova, "Modeling of flux switching permanent magnet machines with Fourier analysis", *IEEE Trans. Magn.*, vol. 46, no. 6, pp. 1499-1502, Jun. 2010.
6. W. Min, J. T. Chen, Z. Q. Zhu, Y. Zhu, M. Zhang, G. H. Duan, "Optimization and comparison of novel E-core and C-core linear switched flux PM machines", *IEEE Trans. Magn.*, vol. 47, no. 8, pp. 2134-2141, Aug. 2011.
7. N. K. Nguyen, F. Meinguet, E. Semail, X. Kestelyn, "Fault-tolerant operation of an open-end winding five-phase PMSM drive with short-circuit inverter fault", *IEEE Trans. Ind. Electron.*, vol. 63, no. 1, pp. 595-605, Jan. 2016.
8. U. B. Akuru, M. J. Kamper, "Formulation and multiobjective design optimization of wound-field flux switching machines for wind energy drives", *IEEE Trans. Ind. Electron.*, vol. 65, no. 2, pp. 1828-1836, Feb. 2018.
9. X. Zhu, Z. Shu, L. Quan, Z. Xiang, X. Pan, "Multi-objective optimization of an outer-rotor V-shaped permanent magnet flux switching motor based on multi-level design method", *IEEE Trans. Magn.*, vol. 52, no. 10, pp. 1-8, Oct. 2016.
10. Z. Xiang, X. Zhu, L. Quan, Y. Du, C. Zhang, D. Fan, "Multilevel design optimization and operation of a brushless double mechanical port flux-switching permanent-magnet motor", *IEEE Trans. Ind. Electron.*, vol. 63, no. 10, pp. 6042-6054, Oct. 2016.
11. X. Zhu, Z. Xiang, C. Zhang, L. Quan, Y. Du, W. Gu, "Co-reduction of torque ripple for outer rotor flux-switching PM motor using systematic multi-level design and control schemes", *IEEE Trans. Ind. Electron.*, vol. 64, no. 2, pp. 1102-1112, Feb. 2017.
12. J. Wang, X. Yuan, K. Atallah, "Design optimization of a surface-mounted permanent-magnet motor with concentrated windings for electric vehicle applications", *IEEE Trans. Veh. Technol.*, vol. 62, no. 3, pp. 1053-1064, Mar. 2013.
13. V. T. Buyukdegirmenci, A. M. Bazzi, P. T. Krein, "Evaluation of induction and permanent-magnet synchronous machines using drive-cycle energy and loss minimization in traction applications", *IEEE Trans. Ind. Appl.*, vol. 50, no. 1, pp. 395-403, Jan. 2014.
14. E. Carraro, M. Morandin, N. Bianchi, "Traction PMASR motor optimization according to a given driving cycle", *IEEE Trans. Ind. Appl.*, vol. 52, no. 1, pp. 209-216, Jan. 2016.
15. A. Fatemi, N. A. O. Demerdash, T. W. Nehl, D. M. Ionel, "Large-scale design optimization of PM machines over a target operating cycle", *IEEE Trans. Ind. Appl.*, vol. 52, no. 5, pp. 3772-3782, Sep. 2016.
16. H. Chen, X. Liu, N. A. O. Demerdash, A. M. EL-Refaie, J. Zhao, J. He, "Comparison and design optimization of a five-phase flux-switching PM machine for in-wheel traction applications", *IEEE Trans. Energy Convers.*.
17. D. M. Ionel, M. Popescu, "Ultrafast finite-element analysis of brushless PM machines based on space-time transformations", *IEEE Trans. Ind. Appl.*, vol. 47, no. 2, pp. 744-753, Mar. 2011.
18. G. Y. Sizov, D. M. Ionel, N. A. O. Demerdash, "Modeling and parametric design of permanent-magnet AC machines using computationally efficient finite-element analysis", *IEEE Trans. Ind. Electron.*, vol. 59, no. 6, pp. 2403-2413, Jun. 2012.
19. P. A. Hargreaves, "Advanced performance prediction tools for the analysis of rotating electrical machines", 2012.
20. M. Ehsani, Y. Gao, A. Emadi, "Fundamentals of vehicle propulsion and brake" in Modern Electric Hybrid Electric and Fuel Cell Vehicles: Fundamentals Theory and Design, Boca Raton, FL, USA:CRC Press, pp. 21-65, 2010.
21. M. J. Li, M. K. Ng, Y. Cheung, J. Z. Huang, "Agglomerative fuzzy K-means clustering algorithm with selection of number of clusters", *IEEE Trans. Knowl. Data Eng.*, vol. 20, no. 11, pp. 1519-1534, Nov. 2008.
22. J. Goss, P. H. Mellor, R. Wrobel, D. A. Staton, M. Popescu, "The design of ac permanent magnet motors for electric vehicles: A computationally efficient model of the operational envelope", *Proc. 6th IET Int. Conf. Power Electron. Mach. Drives*, pp. 1-6, 2012.
23. H. A. Moghaddam, A. Vahedi, S. H. Ebrahimi, "Design optimization of transversely laminated synchronous reluctance machine for flywheel energy storage system using response surface methodology", *IEEE Trans. Ind. Electron.*, vol. 64, no. 12, pp. 9748-9757, Dec. 2017.

24. T. Marčič, B. Štumberger, G. Štumberger, "Differential-evolution-based parameter identification of a line-start IPM synchronous motor", *IEEE Trans. Ind. Electron.*, vol. 61, no. 11, pp. 5921-5929, Nov. 2014.
25. Y. Wang, D. M. Ionel, M. Jiang, S. J. Stretz, "Establishing the relative merits of synchronous reluctance and PM-assisted technology through systematic design optimization", *IEEE Trans. Ind. Appl.*, vol. 52, no. 4, pp. 2971-2978, Jul. 2016.
26. A. Fatemi, D. M. Ionel, N. A. O. Demerdash, D. A. Staton, R. Wrobel, Y. C. Chong, "A computationally efficient method for calculation of strand eddy current losses in electric machines", *Proc. IEEE Energy Convers. Congr. Expo.*, pp. 1-8, 2016.
27. P. Zhang et al., "Multi-objective tradeoffs in the design optimization of a brushless permanent-magnet machine with fractional-slot concentrated windings", *IEEE Trans. Ind. Appl.*, vol. 50, no. 5, pp. 3285-3294, Sep. 2014.
28. P. Zhang, G. Y. Sizov, J. He, D. M. Ionel, N. A. O. Demerdash, "Calculation of magnet losses in concentrated-winding permanent-magnet synchronous machines using a computationally efficient finite-element method", *IEEE Trans. Ind. Appl.*, vol. 49, no. 6, pp. 2524-2532, Nov. 2013.

KEYWORDS

IEEE Keywords

Optimization , Traction motors , Induction motors , Torque , Reluctance motors , Stators INSPEC: Controlled Indexing dynamometers , eddy current losses , finite element analysis , fuel economy , machine theory , magnetic flux , optimisation , permanent magnet motors , response surface methodology , rotors

INSPEC: Non-Controlled Indexing

five-phase outer-rotor flux-switching permanent magnet machine , urban dynamometer driving schedule , highway fuel economy driving schedule , finite-element analysis method , copper losses , computationally efficient optimization , five-phase flux-switching PM machine , in-wheel traction applications , cyclic representative operating points extraction technique , response surface methodology , UDDS-HWFET , PM eddy-current losses , CE-FEA method

Author Keywords

Design optimization , driving cycle , flux-switching , permanent-magnet (PM) machine